Supplemental information

Atomistic Observation and Transient Reordering of Antisited Li/Fe Defects toward Sustainable $LiFePO_4$

Yaqing Guo,[a,b] Yonggang Yao,[a,*] Chi Guo,[c] Yaduo Song,[a] Pengjie Huang,[a] Xiaobin Liao,[d] Kun He,[b] Hao Zhang,[a] Hanwen Liu,[a] Rong Hu,[a] Wei Wang,[b] Cheng Li,[a] Shun Wang,[b] Anmin Nie,[e,*] Yifei Yuan,[b,*] Yunhui Huang[a,*]

a. State Key Laboratory of Materials Processing and Die & Mould Technology, School of Materials Science and Engineering, Huazhong University of Science and Technology, Wuhan, 430074, China

b. College of Chemistry and Materials Engineering, Wenzhou University, Wenzhou, 325035, China

c. Jiangsu Key Laboratory for Design and Manufacture of Micro-Nano Biomedical Instruments, School of Mechanical Engineering, Southeast University, Nanjing, 211189, China

d. State Key Laboratory of Advanced Technology for Materials Synthesis and Processing International School of Materials Science and Engineering, Wuhan University of Technology Wuhan, 430070, China

e. Center for High-Pressure Science, State Key Laboratory of Metastable Materials Science and Technology, Yanshan University, Qinhuangdao, 066004, China

*Correspondence author: Yunhui Huang, Yonggang Yao, Yifei Yuan, Anmin Nie

E-mail: huangyh@hust.edu.cn; yaoyg@hust.edu.cn; yifeiyuan@wzu.edu.cn; anmin@ysu.edu.cn.

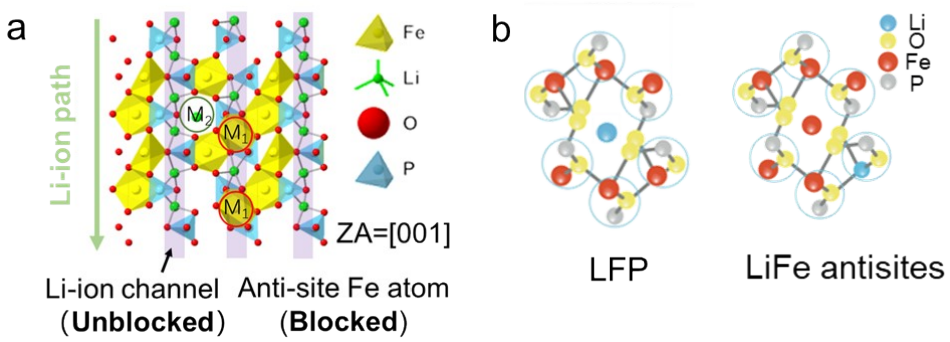

Figure S1. a) Schematic of the LiFe antisites in degraded LFP, M_1 presents to the Fe occupation in Li site (Fe_{Li}) and M_2 presents to the Li occupation in Fe site (Li_{Fe}). b) Schematic of the LFP and LiFe antisite defect hexagonal ring model corresponding to the LFP [010] zone axis observed in STEM.

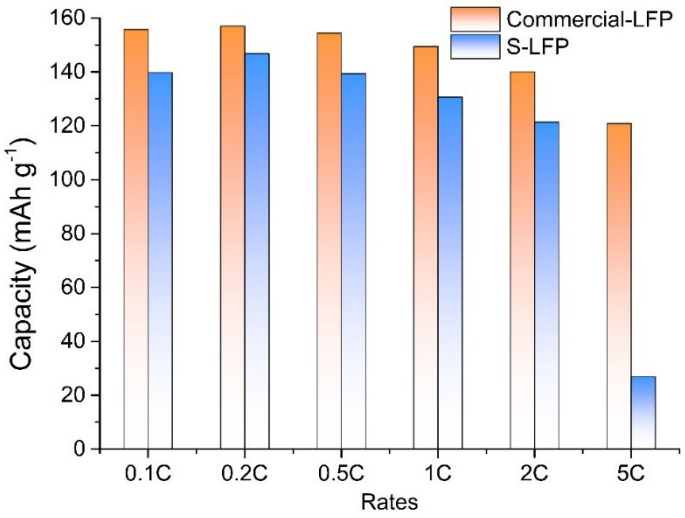

Figure S2. The rate performance of S-LFP and commercial LFP.

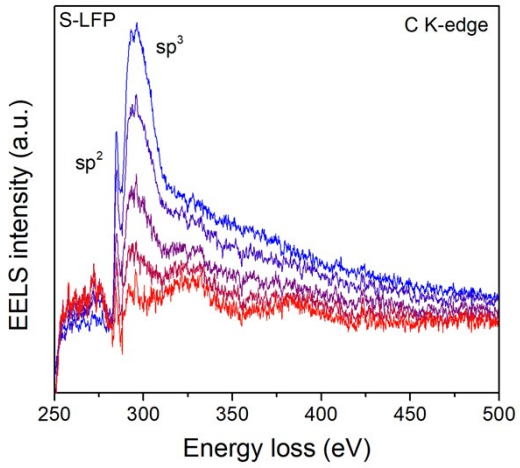

Figure S3. The comparison of C K-edge EELS low-loss spectra between the surface and the interior of S-LFP.

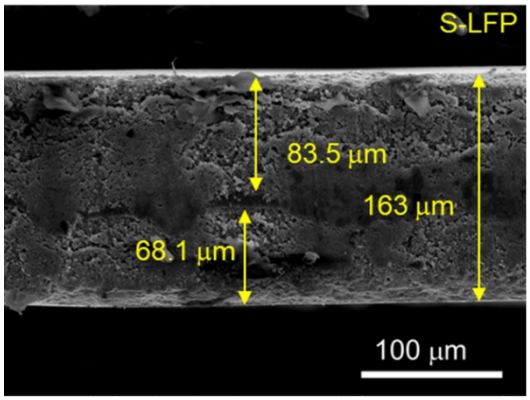

Figure S4. Cross-sectional and surface SEM images of S-LFP electrode.

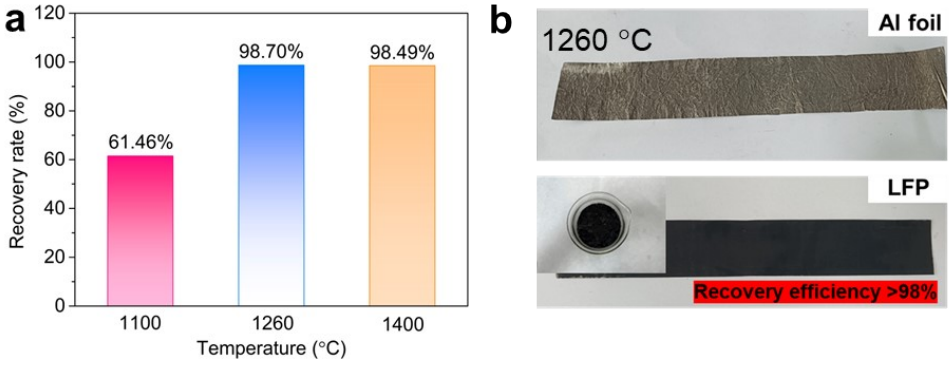

Figure S5. The images depict the Al foil and recovery rate of the LFP after shock-type heating of the electrode. The used electrode sheets were cut into small pieces (1.4 cm × 4.0 cm), and three pieces were averaged. The recovery rate is calculated as the weight of the black powder obtained after separation from each piece divided by the weight of the used electrode sheet minus the weight of the Al foil after separation, multiplied by 100%. The black powder includes LFP, Super P, and carbonized PVDF.

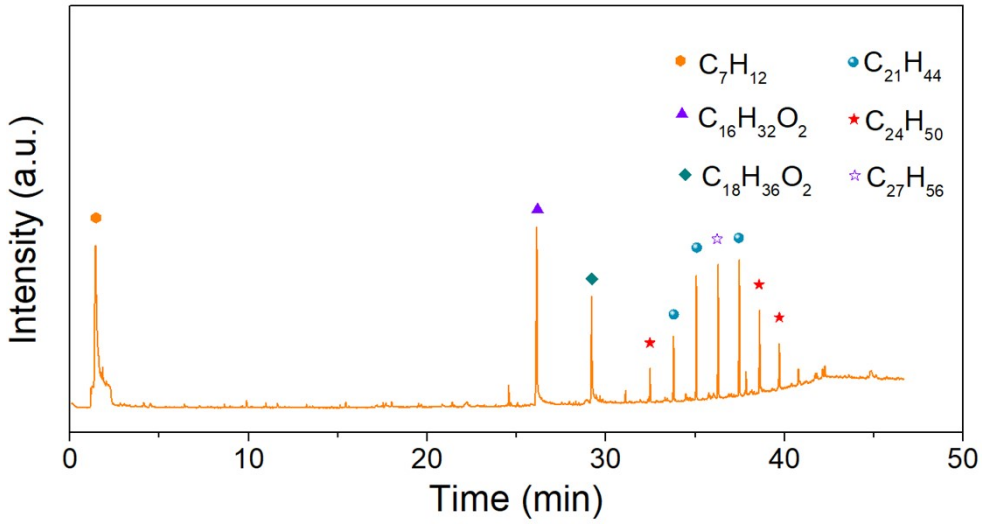

Figure S6. Total ion chromatogram of S-LFP pyrolyzed in Py-GC/MS, demonstrating the binder decomposed components.

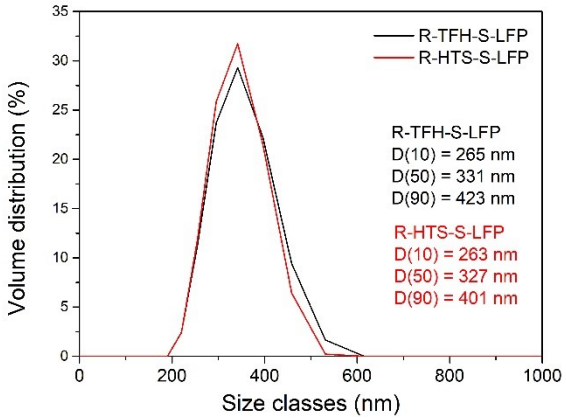

Figure S7. Size distribution of S-LFP electrodes after HTS and TFH treatment.

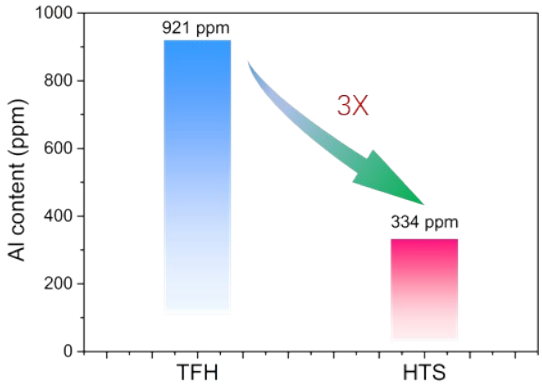

Figure S8. Al impurity content of LFP particles after tube furnace heating reaction (TFH) and shock-type heating.

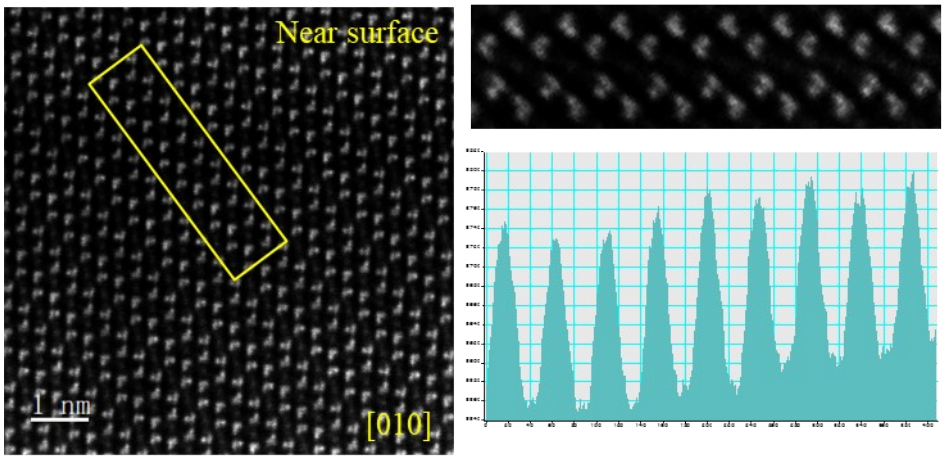

Figure S9. HAADF STEM image and the intensity line profile along the yellow box in [010] orientation of R-HTS-S-LFP.

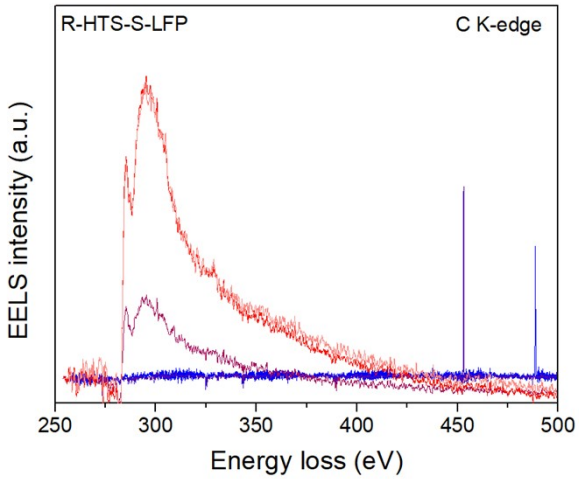

Figure S10. The comparison of C K-edge EELS low-loss spectra between the surface and the interior of R-HTS-S-LFP.

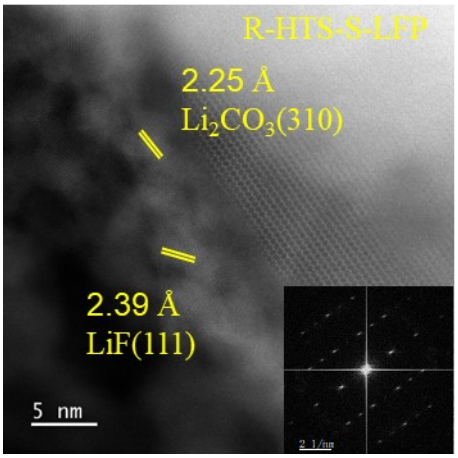

Figure S11. HAADF STEM of the surface of R-HTS-S-LFP in [010] orientation.

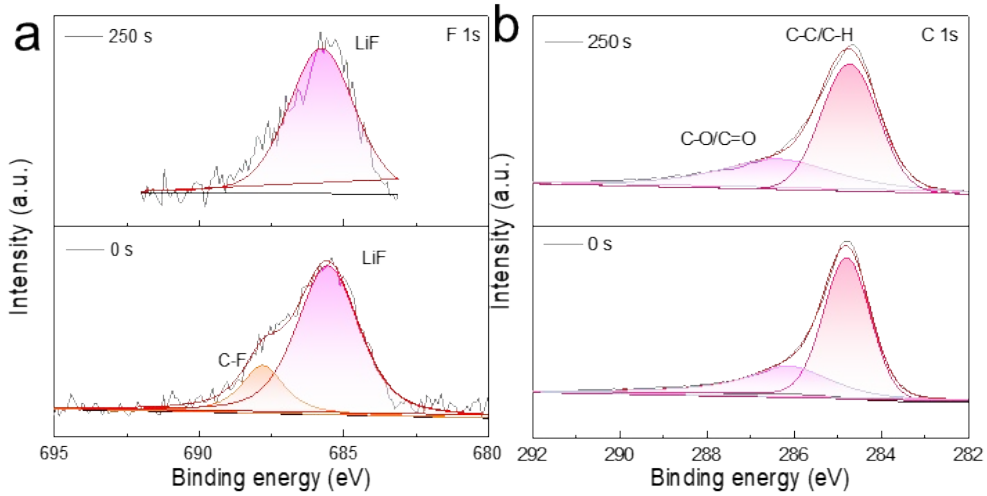

Figure S12. a) C 1s and b) F 1s XPS spectrum of R-HTS-S-LFP.

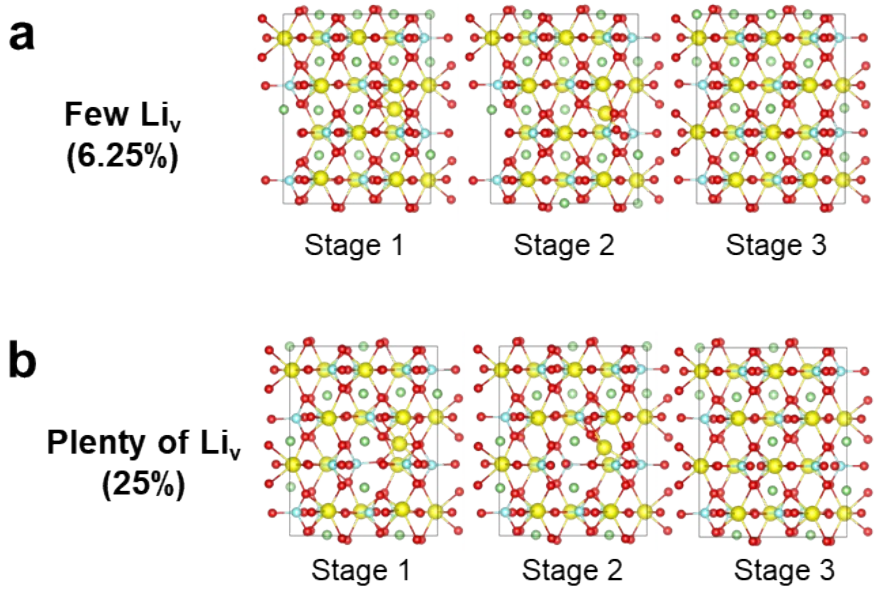

Figure S13. Corresponding crystallographic information file from different stages of LFP with a) few Li_V and b) plenty of Li_V.

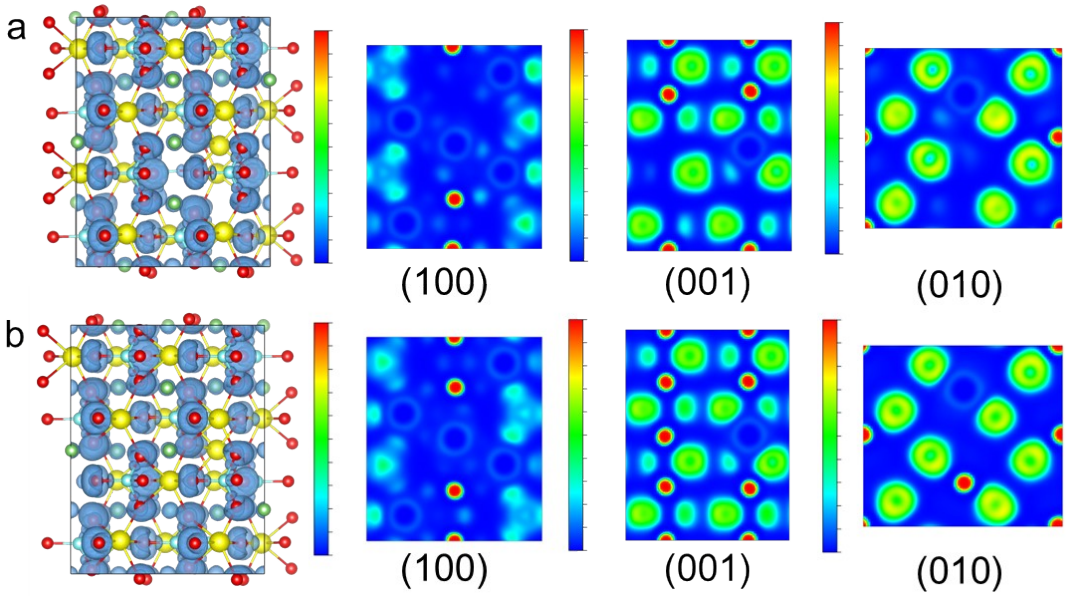

Figure S14. Corresponding 2D electron localization function contour plot of Fe for a) LFP with 25% Li_{Vs} and b) LFP with 6.25% Li_{Vs}.

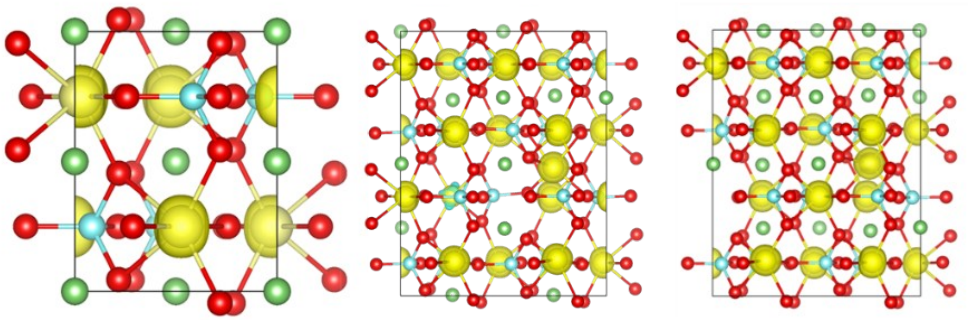

Figure S15. The spin density of the element Fe for original LFP, LFP with 25% Li_{Vs} and LFP with 6.25% Li_{Vs}.

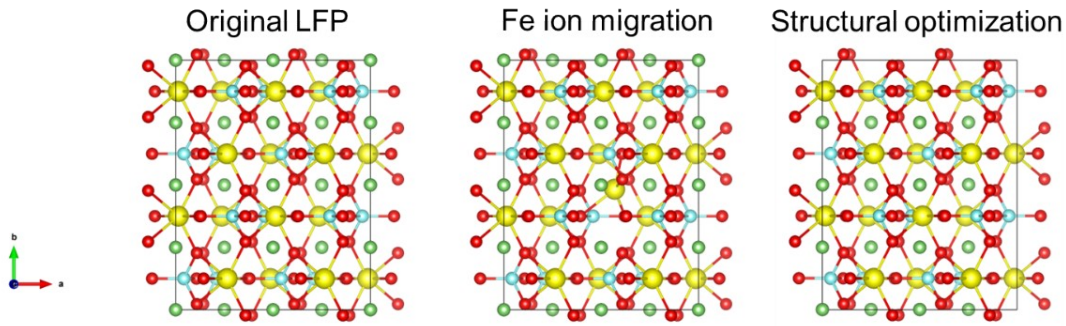

Figure S16. In the R-HTS-S-LFP structure, Fe undergoes further Li/Fe anti-site exchanges and structural optimization. The results indicate that in a perfect crystal without Li vacancies, Fe returns to its original sites rather than occupying Li sites.

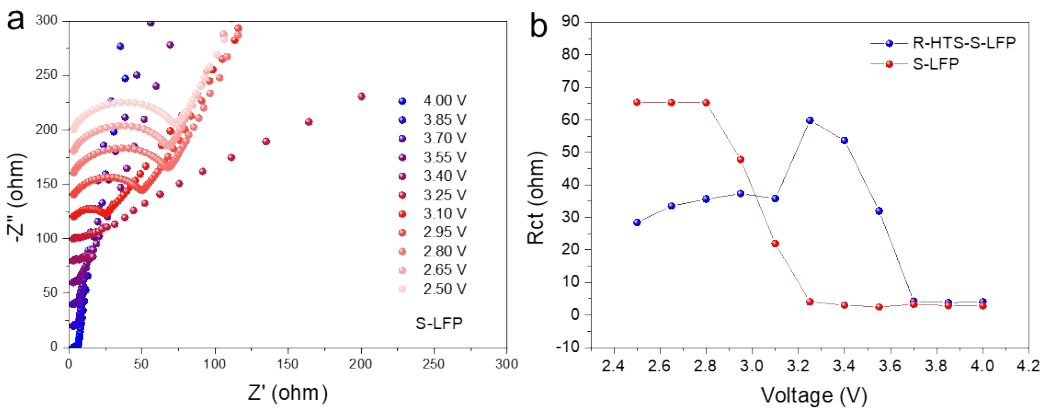

Figure S17. *In-situ* EIS for a) S-LFP and b) EIS fitting results for S-LFP and R-HTS-S-LFP.

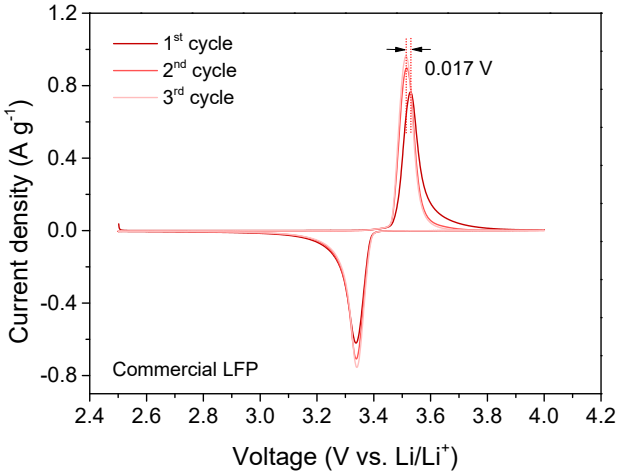

Figure S18. The CV curves of the commercial LFP with the scan rate of 0.1 mV s^{-1}.

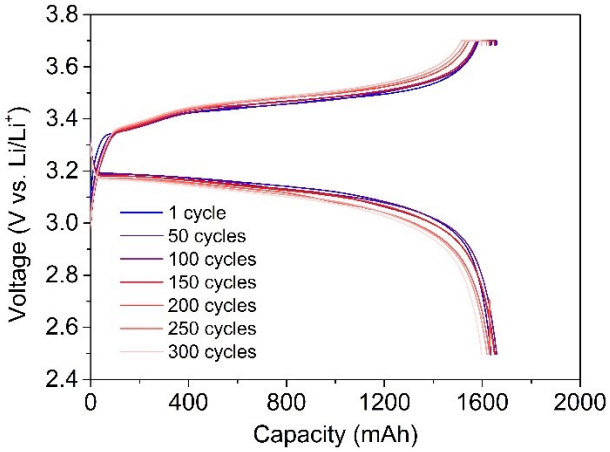

Figure S19. The charge-discharge curves of R-HTS-S-LFP for different cycles

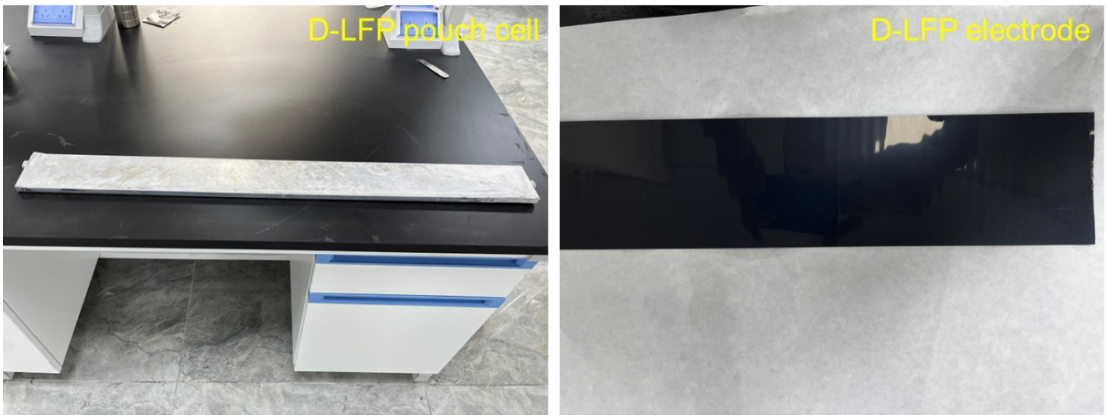

Figure S20. The pouch cell and electrode of D-LFP.

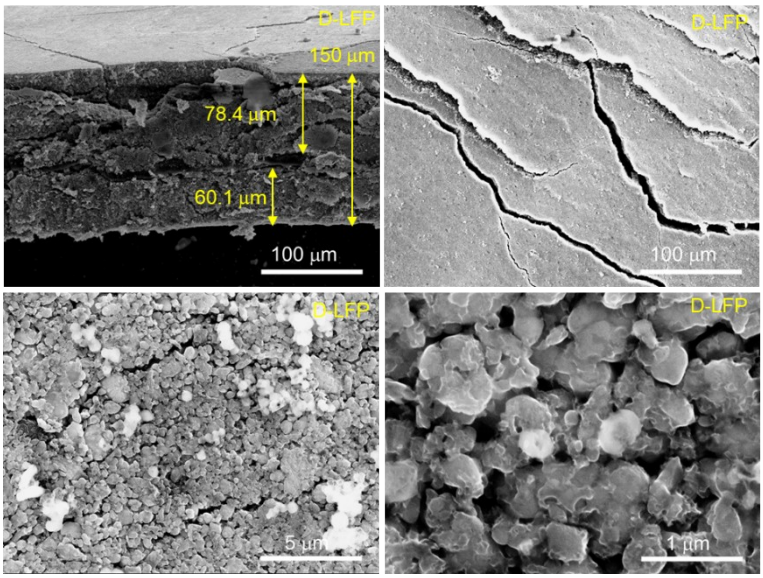

Figure S21. SEM images of D-LFP electrode.

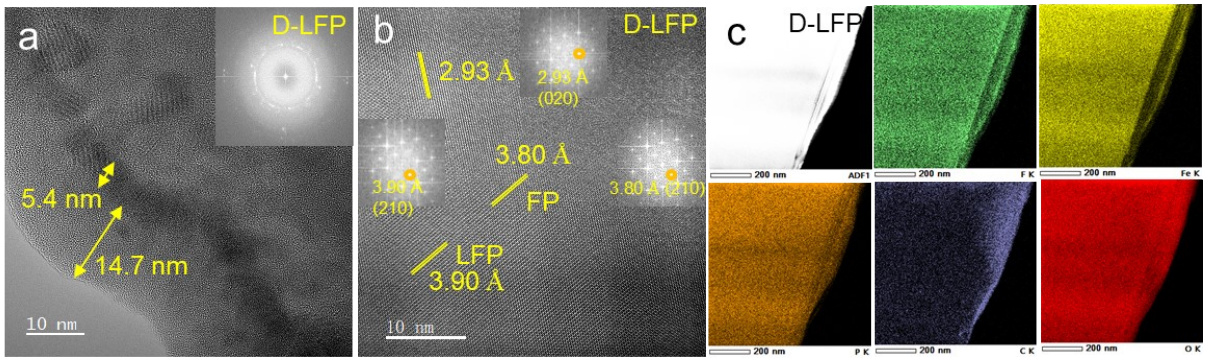

Figure S22. TEM images and EDS mapping of D-LFP electrode.

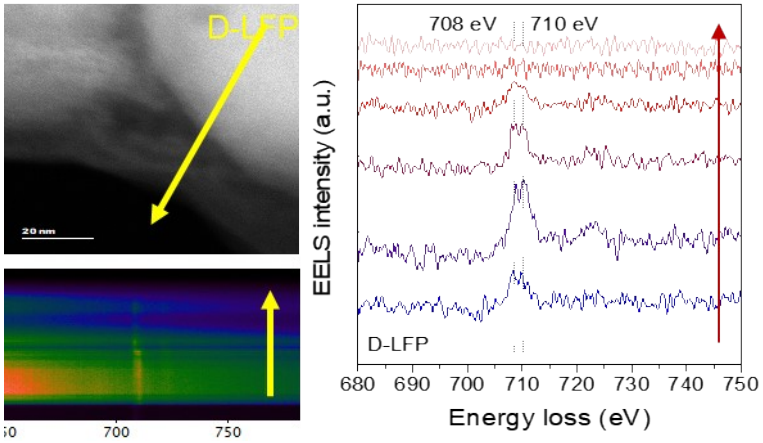

Figure S23. The comparison of EELS low-loss spectra between the surface and the interior of D-LFP.

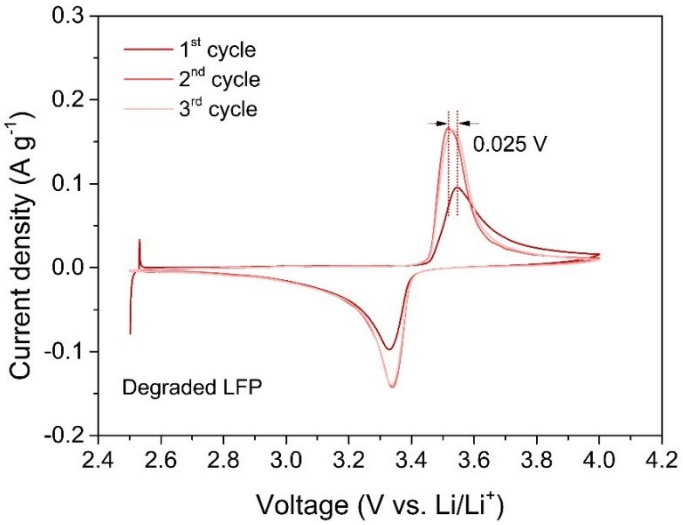

Figure S24. The CV curves of D-LFP.

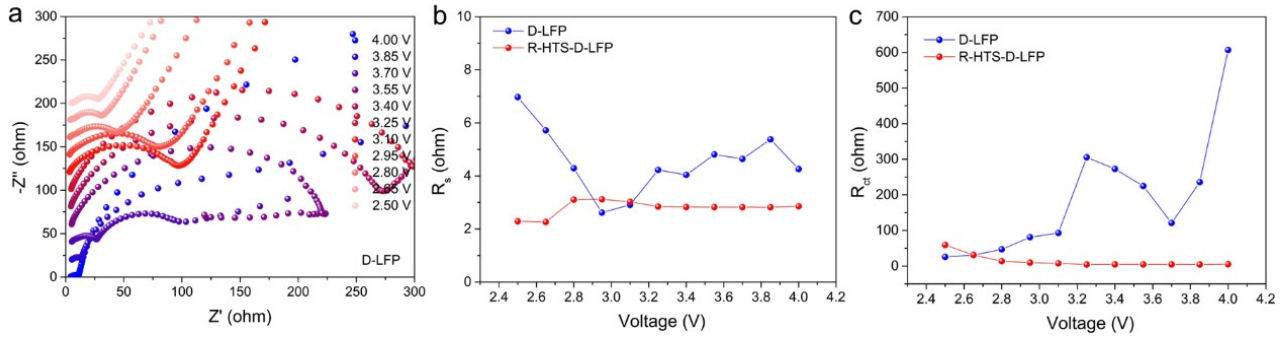

Figure S25. *In-situ* EIS for a) D-LFP and EIS fitting results of b) R_s and c) R_{ct} for D-LFP and R-HTS-DD-LFP.

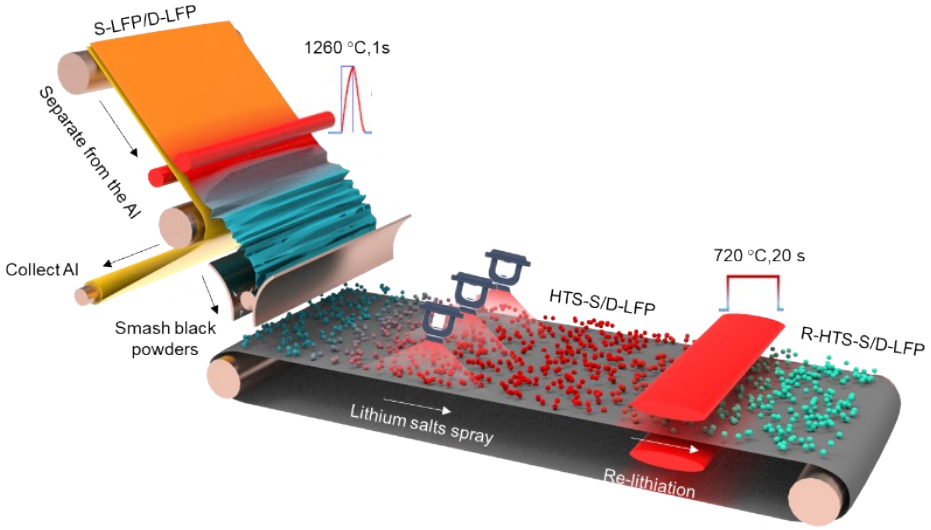

Figure S26. Schematic diagram of transient reordering of antisited Li/Fe defects for sustainable industrial production of LFP.

Supporting Table 1: The samples and how they were obtained.

Category	Abbreviations	Full name	Description of obtaining method
Spent materials	S-LFP	Scrap $LiFePO_4$	Scrap $LiFePO_4$ without cycling
	D-LFP	Degraded $LiFePO_4$	Degraded $LiFePO_4$ with cycling
HTS-treated materials	HTS-S-LFP	High-temperature shock scrap $LiFePO_4$	Separated from scrap $LiFePO_4$ electrode by high-temperature shock (1260 °C/1 s in Ar)
	HTS-D-LFP	High-temperature shock degraded $LiFePO_4$	Separated from degraded $LiFePO_4$ electrode by high-temperature shock (1260 °C/1 s in Ar)
Regenerated materials	R-HTS-LFP	Regenerated high-temperature shock scrap $LiFePO_4$	Regenerated LiOH coated HTS-S-LFP through high temperature shock treatment (720 °C/20 s in Ar)
	R-HTS-D-LFP	Regenerated high-temperature shock degraded $LiFePO_4$	Regenerated LiOH coated HTS-D-LFP through high temperature shock treatment (720 °C/20 s in Ar)

Supporting Table 2: Structural parameters obtained from Rietveld refinement of XRD pattern of S-LFP. Phase $LiFePO_4$: Space group: *Pnma*, R_{wp} = 3.43%, a = 10.32940(5) Å, b = 6.00660(27) Å, c = 4.69313(25) Å, $\alpha = \beta = \gamma = 90°$.

Atom	Site	Wyckoff positions			Occupancy
Li	4a	0	0	0	0.9469
Fe	4a	0	0	0	0.0531
Fe	4c	0.2822	0.2500	0.9749	0.9469
Li	4c	0.2822	0.2500	0.9749	0.0531
P	4c	0.0950	0.2500	0.4183	1.0000
O	4c	0.0971	0.2500	0.7431	1.0000
O	4c	0.4573	0.2500	0.2054	1.0000
O	8d	0.1657	0.0467	0.2852	1.0000

Supporting Table 3: Structural parameters obtained from Rietveld refinement of XRD pattern of HTS-S-LFP. Phase $LiFePO_4$: Space group: *Pnma*, R_{wp} = 3.53%, a = 10.33947(27) Å, b = 6.00780(15) Å, c = 4.69386(14) Å, $\alpha = \beta = \gamma = 90°$.

Atom	Site	Wyckoff positions			Occupancy
Li	4a	0	0	0	0.9570
Fe	4a	0	0	0	0.0427
Fe	4c	0.2822	0.2500	0.9747	0.9570
Li	4c	0.2822	0.2500	0.9747	0.0427
P	4c	0.0948	0.2500	0.4187	1.0000
O	4c	0.0987	0.2500	0.7435	1.0000
O	4c	0.4484	0.2500	0.2045	1.0000
O	8d	0.1661	0.0433	0.2853	1.0000

Supporting Table 4: Structural parameters obtained from Rietveld refinement of XRD pattern of R-HTS-S-LFP. Phase $LiFePO_4$: Space group: *Pnma*, R_{wp} = 3.27%, a = 10.34005(19) Å, b = 6.00816(11) Å, c = 4.69416(10) Å, $\alpha = \beta = \gamma = 90°$.

Atom	Site	Wyckoff positions			Occupancy
Li	4a	0	0	0	0.9731
Fe	4a	0	0	0	0.0269
Fe	4c	0.2822	0.2500	0.9747	0.9731
Li	4c	0.2822	0.2500	0.9747	0.0269
P	4c	0.0948	0.2500	0.4187	1.0000
O	4c	0.0973	0.2500	0.7467	1.0000
O	4c	0.4561	0.2500	0.2043	1.0000
O	8d	0.1676	0.0410	0.2889	1.0000

Supporting Table 5: The total charge of Fe with different samples.

Samples		Original LFP	LFP with 8 Li_v	LFP with 1 Li_v
A total charge of Fe	1	6.578	6.478	6.379
	2	6.578	6.565	6.663
	3	6.578	6.572	6.577
	4	6.578	6.671	6.576
	5	6.578	6.403	6.602
	6	6.578	6.496	6.572
	7	6.578	6.573	6.593
	8	6.578	6.592	6.602
	9	6.578	6.551	6.558
	10	6.578	6.573	6.610
	11	6.578	6.569	6.585
	12	6.578	6.563	6.579
	13	6.578	6.597	6.622
	14	6.578	6.594	6.569
	15	6.578	6.572	6.595
	16	6.578	6.581	6.584
Average		6.578	6.559375	6.579125